

The relationship between the turnover frequency and photo-ionisation in radio sources

S. J. Curran*

School of Chemical and Physical Sciences, Victoria University of Wellington, PO Box 600, Wellington 6140, New Zealand

Accepted —. Received —; in original form —

ABSTRACT

We investigate the connection between the turnover frequency in the radio spectrum, ν_{TO} , and the rate of ionising ultra-violet photons, Q_{HI} , in extragalactic sources. From a large, optically selected, sample we find ν_{TO} to be correlated with Q_{HI} in sources which exhibit a turnover. The significance of the correlation decreases when we include power-law radio sources as limits, by assuming that the turnover frequency occurs below the lowest value observed. However, the power-law fit sources are less well sampled across the band and so these may just be contributing noise to the data. Given that the observed $\nu_{\text{TO}}-Q_{\text{HI}}$ correlation is purely empirical, we use the ionising photon rate to obtain the electron density in a free-free absorption model. For each of the constant, exponential, constant plus exponential (Milky Way) and spherical models of the gas distribution, there is also an increase in the turnover frequency with ionising photon rate. Furthermore, for a given gas mass, we find that the turnover frequency is anti-correlated with the scale-factor of the gas density. While other mechanisms, such as ageing electrons or synchrotron self-absorption, may be required to reproduce the spectral indices, for an exponential scale-factor similar to the linear size, this simple free-free absorption model reproduces the turnover– size correlation seen in radio sources.

Key words: Radio continuum: galaxies – quasars: general – galaxies: active – galaxies: high-redshift – ultraviolet: galaxies

1 INTRODUCTION

High-frequency peaked/gigahertz peaked-spectrum (HFP/GPS) and compact steep-spectrum (CSS) sources form a class of radio source which exhibit a peak in their radio spectrum, while the emission appears to be confined to a small region. Specifically HFPs and GPSs have projected linear sizes of $\ell \lesssim 1$ kpc and peak in their luminosity at a turnover frequency of $\nu_{\text{TO}} \sim 0.4 - 5$ GHz, whereas CSSs have $\ell \gtrsim 10$ kpc and $\nu_{\text{TO}} \lesssim 0.5$ GHz. This reflects the well established anti-correlation between ν_{TO} and ℓ (Fanti et al. 1990; O’Dea & Baum 1997; O’Dea 1998).

The main competing hypotheses for the nature of these are

- (i) that the more compact sources are young and will evolve into the larger CSSs (Fanti et al. 1995),
- (ii) that all of the sources are due to confinement of the radio jets by a dense interstellar medium (the “frustrated” model, O’Dea et al. 1991),
- (iii) or a combination of both (e.g. Bicknell et al. 1997; Begelman 1999; Callingham et al. 2017).

The main issue with the youth argument is the apparent under-abundance of the larger active galactic nucleus (AGN) population into which they canonically evolve (Readhead et al. 1996;

O’Dea & Baum 1997; An & Baan 2012). However, there is mounting evidence that, in addition to frustrated sources and those which will evolve, many of the “young” sources are transient with their radio activity being cyclic on a time-scale of ~ 1000 yr (An & Baan 2012; Callingham et al. 2015, 2017; O’Dea & Saikia 2021).

The large rotation measure in some compact radio sources suggests the presence of large magnetic fields (e.g. Kato et al. 1987), indicating that the radio emission is synchrotron in nature (e.g. Bicknell et al. 1997). However, the majority show only weak polarisation (Stanghellini et al. 1998), which may therefore favour free-free absorption as the dominant mechanism (e.g. Marr et al. 2014; Tingay et al. 2015; Keim et al. 2019), although Bicknell et al. suggest that a large number of magnetic field reversals could keep the net polarisation low.

The dominance of the electron density (free-free absorption) is supported by anti-correlation between the neutral gas abundance, as traced through absorption of the 21-centimetre transition of hydrogen (H I), and turnover frequency in 196 $z \geq 0.1$ radio sources (Curran et al. 2019): The detection rate of H I 21-cm absorption is also strongly anti-correlated with the photo-ionisation rate, Q_{HI} , (Curran et al. 2008; Curran & Whiting 2012). where Q_{HI} drives the electron density.

Thus, we were interested to test whether any of the nine $z = 5.6 - 6.6$ quasars, in which only one had evidence of a possible turnover (Gloude-mans et al. 2023), have relatively low ionising

* Stephen.Curran@vuw.ac.nz

photon rates. However, sufficient rest-frame ultra-violet photometry was available for only one source, which did in fact have an ionising rate well below the cut-off where neutral gas has ever been detected ($Q_{\text{HI}} \approx 3 \times 10^{56} \text{ s}^{-1}$). This is therefore consistent with the argument that no turnover is evident due to a low ionisation rate and, thus, a low electron density.

However, given that this is a single source, to ensure a sample with more comprehensive ultra-violet data, we also searched the photometry of a larger, optically selected sample. From this we find a positive correlation between the turnover frequency and ionising rate, which is supported by a theoretical model. The model also yields an anti-correlation between the turnover frequency and the scale-length of the gas density, which could naturally explain the observed $\nu_{\text{TO}}-\ell$ anti-correlation.

2 THE OBSERVED $\nu_{\text{TO}} - Q_{\text{HI}}$ CORRELATION

2.1 Photometry and fitting

We follow the same procedure as described in Curran et al. (2013), where the data were scraped from the *NASA/IPAC Extragalactic Database* (NED)¹, the *Wide-Field Infrared Survey Explorer* (WISE, Wright et al. 2010) *Two Micron All Sky Survey* (2MASS, Skrutskie et al. 2006) and the *Galaxy Evolution Explorer* (GALEX, data release GR6/7)² databases. For the Gloude-mans et al. (2023) sources the radio data from NED were supplemented with 54 MHz to 3 GHz photometry from Callingham et al. (2017); Slob et al. (2022); Gloude-mans et al. (2022). After shifting the data back into the source’s rest-frame, each flux density measurement, S_ν , was then converted to a specific luminosity, via $L_\nu = 4\pi D_L^2 S_\nu / (z + 1)$, where D_L is the luminosity distance to the source.³

After the removal of duplicate measurements at exactly the same frequency, where there were at least three radio measurements, we applied both log-space first and second order polynomial fits to the data, selecting that which gave the lowest sum residual, $\sum(L_{\text{data}} - L_{\text{fit}})^2$, Fig. 1. If there were less than three measurements the source was not used. Note that the 2nd order fit sources which gave a turnover frequency below the minimum observed were re-fitted with a power law. We used the values from the polynomial as the initial guesses to a GPS-fit function (equation 1 of Snellen et al. 1998). However, due to the limited number of well separated radio photometry points, the bunching of the data at similar frequencies gave much more disparate fits. The polynomial fitting appeared to be more robust, mostly giving reasonable agreement with the GPS-fits, and better agreement with those of O’Dea & Baum (1997).⁴

The ionising ($\lambda \leq 912 \text{ \AA}$) photon rate was determined from the rest-frame UV luminosities, via (Osterbrock 1989)

$$Q_{\text{HI}} \equiv \int_{\nu_{\text{ion}}}^{\infty} \frac{L_\nu}{h\nu} d\nu, \quad (1)$$

where ν is the frequency (with $\nu_{\text{ion}} = 3.29 \times 10^{15} \text{ Hz}$ for H I) and h the Planck constant. Again, requiring at least three photometry measurements, fitting the rest-frame UV data with a power-law fit, $L_\nu \propto \nu^\alpha$, gives

$$\log_{10} L_\nu = \alpha \log_{10} \nu + C, \quad (2)$$

¹ See Appendix A.

² <http://galex.stsci.edu/GR6/#mission>

³ We use $H_0 = 67.4 \text{ km s}^{-1} \text{ Mpc}^{-1}$ and $\Omega_m = 0.3125$ (Planck Collaboration et al. 2020) throughout the paper.

⁴ See Appendix B.

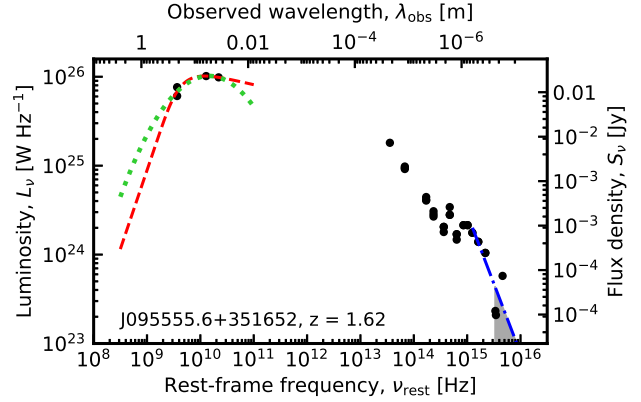


Figure 1. Example of the photometry fitting (from the SDSS sample, Sect. 2.2.2). The radio fits are shown as the dotted (polynomial) and dashed (GPS-fit) curves and the UV as the power-law fit. The shaded region shows $\nu \geq 3.29 \times 10^{15} \text{ Hz}$, over which the ionising photon rate is calculated. For the GPS-fit shown $\alpha_{\text{thick}} = 1.77$ and $\alpha_{\text{thin}} = -0.14$.

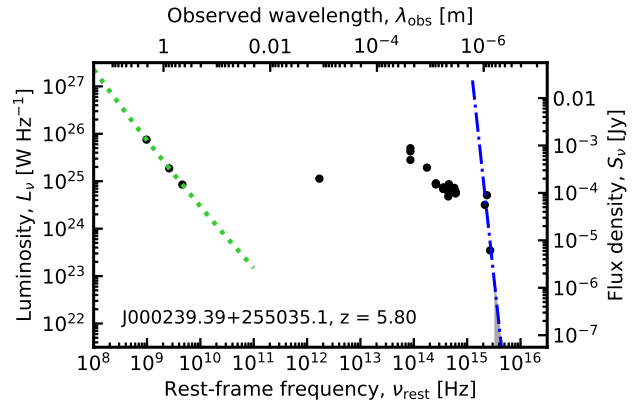


Figure 2. The rest-frame photometry of the one source of Gloude-mans et al. which had sufficient UV data to yield Q_{HI} . These are from the Pan-STARRS1 i, z, y bands (Bañados et al. 2014) and the radio data from Gloude-mans et al. (2023).

where C is the log-space intercept and α the gradient (the UV spectral index, see Fig. 1). Integrating this over ν_{ion} to ∞ gives the ionising photon rate as

$$Q_{\text{HI}} = \frac{-10^C}{\alpha h} \nu_{\text{ion}}^\alpha, \quad (3)$$

which was then calculated for each source with sufficient rest-frame UV photometry.

2.2 Samples

2.2.1 The Gloude-mans et al. sample

As stated above, only one source, J0002+2550 (WISEA J000239.39+255035.1), had sufficient rest-frame UV data to determine the ionising photon rate.⁵ This is shown in Fig. 2, from which we obtain an ionising rate of $Q_{\text{HI}} = 9.3 \times 10^{54} \text{ s}^{-1}$.

⁵ Of the remaining eight, only four had any rest-frame IR–UV photometry and are shown in Appendix C.

This is well below the $\approx 3 \times 10^{56} \text{ s}^{-1}$ limit at which all of the gas in the host galaxy is believed to be ionised (Curran & Whiting 2012) and well within the regime where HI 21-cm absorption has been detected (Curran et al. 2008, 2019).

Thus, for the one source for which we could obtain the photometry, the absence of a turnover in the radio SED is consistent with a relatively low ionisation fraction. We do note, however, that this has an unusually steep spectral index in the UV band ($\alpha_{\text{UV}} = -10.37$) and whether this applies to the other eight sources in the sample we cannot comment. At such high redshifts we would expect a steepening of the spectral index due to intervening hydrogen, specifically the Lyman- α forest (e.g. Janknecht et al. 2002; Barger & Cowie 2010) and Lyman Limits systems (e.g. Mo et al. 2010). In Fig. 2, $\lambda = 1216 \text{ \AA}$ occurs immediately after the second highest frequency point and so the above ionising photon rate should be treated as a lower limit (see Sect. 3.2).

In order to investigate the relation between the ionising photon rate and turnover frequency, we turned to a large sample, which is optically selected in order to increase the likelihood of yielding the necessary rest-frame UV photometry.

2.2.2 The SDSS sample

We use the sample of Curran et al. (2021), which comprises the first 100 000 QSOs of the SDSS Data Release 12 (DR12, Alam et al. 2015) with accurate redshifts. From these we shortlisted the sources which had at least one flux measurement below 10 GHz, giving 3429 radio sources. As stated above, we required at least three flux measurements to fit the radio data, which gave 1005 sources of which 499 could be fit. Of these, the ionising photon rate could be obtained for 416 source, of which 257 sources which were fit by a power law with 159 exhibiting a turnover. Since we are primarily interested in the turnover frequency, we used the polynomial results in the following analysis.

In order to supplement the radio data, we added photometry compiled in surveys with the *Galactic and Extragalactic All-sky Murchison Widefield Array* (GLEAM), specifically:

- (i) The 1483 sources with $72 \leq \nu_{\text{TO}} \leq 1400 \text{ Mz}$ (Callingham et al. 2017).
- (ii) The 373 sources of Slob et al. (2022), of which 36 exhibit $\nu_{\text{TO}} \sim 150 \text{ Mz}$.
- (iii) The 24 high redshift ($4.9 \leq z \leq 6.6$) radio bright sources of Gloudemans et al. (2022).

Of the first two samples, spectroscopic redshifts were available for 214 and 49 sources, respectively. Comparing these with the SDSS sample gave just a single match, [HB89] 1252+119 (GLEAM J125438+114103) at $z = 0.872$.⁶ The lowest observed rest-frame frequency is 141 MHz, compared to 676 MHz for the NED only data. For the low frequency plus NED photometry, the polynomial fit gives $\nu_{\text{TO}} = 10^{9.36 \pm 0.03} \text{ Hz} = 2.29_{-0.07}^{+0.23} \text{ GHz}$ and the GPS fit 251 MHz (Fig. 3), whereas the NED only data gives $\nu_{\text{TO}} = 10^{8.40 \pm 1.70} \text{ Hz} = 252_{-247}^{+12400} \text{ MHz}$ and the GPS fit

⁶ Note that there are two other coordinate matches, [HB89] 1307+121 (GLEAM J130934+115425) and [HB89] 1442+101 (GLEAM J144516+095835), although the redshifts of the SDSS and GLEAM sources are very different – $z = 2.6006$, cf. 0.34286 and $z = 3.5203$, cf. 0.25578, respectively.

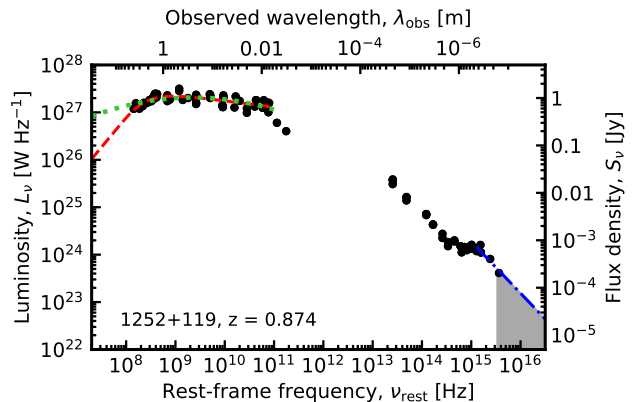


Figure 3. The rest-frame photometry of the one SDSS source which was common to the low frequency catalogues (from the peaked-spectrum sources of Callingham et al. 2017).

603 MHz⁷. This is actually closer to the $\nu_{\text{TO}} = 608 \text{ MHz}$ of Callingham et al. (2017)⁸ which uses the low frequency data.

2.2.3 The low frequency samples

We also performed full photometry searches on the low frequency samples. Of the sources with at least three radio photometry measurements, 260 have spectroscopic redshifts, of which 24 were best fit by a power law and 201 with a turnover.⁹ Just 55 of these had sufficient rest-frame UV photometry to obtain the ionising photon rate and adding these to the SDSS sources with a measured Q_{HI} , gave 263 first order fit sources and 208 second order fit.

2.3 Selection effects

2.3.1 Radio flux limits

In Fig. 4 we show the radio and UV luminosity distributions of the combined SDSS plus low frequency sample. The UV and radio luminosities are strongly correlated, with a Kendall-tau test giving a probability of $p(\tau) = 9.20 \times 10^{-13}$ of this arising by chance, which is significant at $Z(\tau) = 7.14\sigma$, assuming Gaussian statistics. Also, it is apparent that the 1st order fit sources are generally more luminous at $\lambda = 21 \text{ cm}$ than those with a 2nd order fit.

This could be due to the flagging of 2nd order fits as 1st order if the fitted turnover frequency is below the minimum observed, which will have the effect of boosting the luminosity if the putative turnover occurs at $\nu_{\text{TO}} < 1.4 \text{ GHz}$. This may be evident in Fig. 5, where the 2nd order fit sources are, on average, more fully sampled, thus making it possible that some of the 1st order fit sources may exhibit a turnover if sampled to a similar degree. The median radio bandwidths of the low frequency observations is $\Delta\nu \sim 750 \text{ MHz}$ (Callingham et al. 2017; Slob et al. 2022) and so we remove our most extreme outliers (at $\Delta\nu \lesssim 1 \text{ GHz}$) from the sample in the following analysis.

⁷ Which, being lower than the minimum observed frequency, would be fitted with a power law.

⁸ 325 MHz in the observed frame (J. Callingham, private communication).

⁹ Although the remaining 35 appeared to be amply sampled, some gave inverted spectra and the bunching of data at similar frequencies in others prevented a fit.

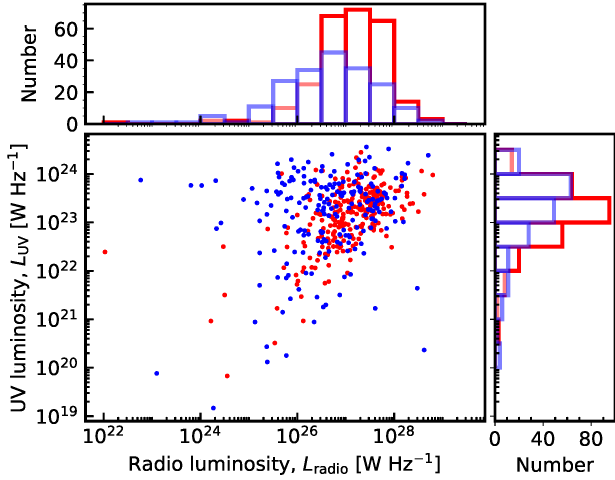


Figure 4. The UV ($\lambda = 912 \text{ \AA}$) and radio ($\lambda = 21 \text{ cm}$) luminosities of the SDSS plus low frequency samples. For the 1st order fit sources (red markers/histogram) the mean luminosities are $\langle \log_{10} L_{\text{radio}} \rangle = 27.08 \pm 0.75$ and $\langle \log_{10} L_{\text{UV}} \rangle = 23.15 \pm 0.65$ and for the 2nd order (blue markers/histogram) fit sources, $\langle \log_{10} L_{\text{radio}} \rangle = 26.61 \pm 0.98$ and $\langle \log_{10} L_{\text{UV}} \rangle = 23.14 \pm 0.93$. A t -test gives a probability of $p(t) = 9.61 \times 10^{-9}$ that the mean radio luminosities are the same and $p(t) = 0.911$ that the mean UV luminosities are the same.

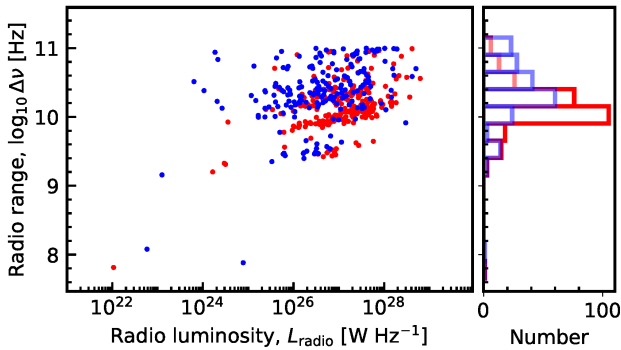


Figure 5. The frequency spans of the SDSS plus low frequency samples, defined as $\log_{10} \Delta\nu = \log_{10}(\nu_{\text{max}} - \nu_{\text{min}})$ up to our 100 GHz cut. For the 1st order fit (red markers/histogram) sources $\langle \log_{10} \Delta\nu \rangle = 10.15 \pm 0.35$ and for the 2nd order fit (blue markers/histogram) sources $\langle \log_{10} \Delta\nu \rangle = 10.35 \pm 0.47$. A t -test gives a probability of $p(t) = 9.55 \times 10^{-8}$ (5.34) that the mean sampled frequency spans are the same.

2.3.2 UV photometry correction

As discussed in Sec. 2.2.1, the higher the redshift the more we expect the rest-frame UV continuum to be absorbed by intervening hydrogen. In the top panel of Fig. 6, we can see a clear Malmquist bias, where the volume probed at low redshift is insufficient to detect the rare high luminosity sources, while at high redshift only the high luminosity sources are detected. We therefore use the spectral index to quantify a correction for the intervening hydrogen. In Fig. 7 we show all of the SDSS sources for which we could obtain an ionising photon rate, from which we can see a steepening in the spectral index with redshift. A linear fit gives

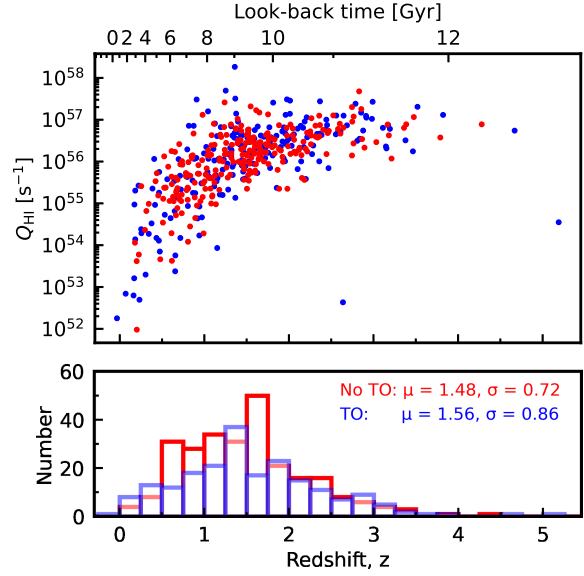


Figure 6. The ionising photon rate versus redshift for the SDSS radio plus low frequency source samples. The red markers/histogram are the power-law (No TO) radio sources and the blue markers/histogram those exhibiting a turnover (TO). The mean values and associated standard deviations are given in the lower panel. A t -test gives a probability of $p(t) = 0.271$ that the mean redshifts are the same.

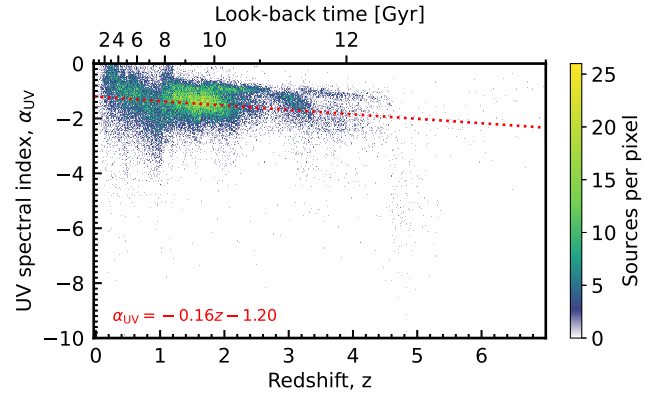


Figure 7. The distribution of the UV spectral index with redshift for the SDSS sources for which the ionising photon rate could be obtained. The dotted line shows the best linear fit.

$\alpha_{\text{UV}} = -0.16z - 1.20$, so, on the basis that the intrinsic spectral index is $\alpha_{\text{UV}} = -1.20$ at $z \sim 0$, we correct each measured value of α_{UV} by subtracting $-0.16z$ (Fig. 8).¹⁰ Although not valid for an individual source, using this to correct the UV spectral index to obtain the intrinsic value provides a statistical correction for the redshift, and thus a better estimate of the ionising photon rate before the absorption of the UV continuum by intervening gas.¹¹

¹⁰ $\alpha_{\text{UV}} = -1.20$ at $z \sim 0$ is similar to values in the literature, e.g. $\alpha_{\text{UV}} = -1.4$ at $z < 1.44$ (Shull et al. 2012) and $\alpha_{\text{UV}} = -1.7$ at $\langle z \rangle = 1$ (Telfer et al. 2002).

¹¹ There is also the issue of dust suppressing the shorter wavelengths in the rest-frame, leading to underestimates in Q_{HI} . However, intrinsic dust will also provide shielding for the gas countering the degree of ionisation somewhat.

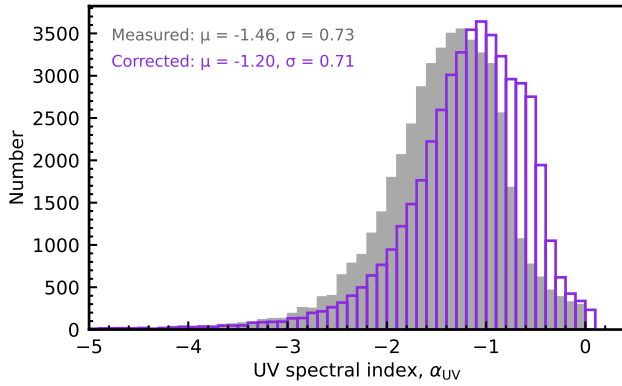


Figure 8. The distribution of the UV spectral index before correction (unfilled histogram) and after correction (filled histogram).

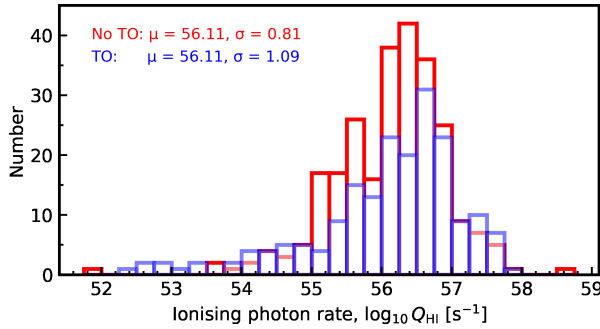


Figure 9. The distribution of the corrected ionising photon rates for the radio sources fit by a power-law (No TO) and exhibiting a turnover (TO).

2.4 Ionising photon rate and turnover frequency

2.4.1 Correlations

From the corrected spectral indices we recalculate the ionising photon rates, according to Equ. 3. Showing these in Fig. 9, we see little difference between the 1st and 2nd order fit sources. A t -test gives a probability of $p(t) = 0.952$ of the mean Q_{HI} values being the same and a Kolmogorov-Smirnov test gives $p(KS) = 0.032$ of the populations being drawn from the same sample.¹²

In Fig. 10 we show the turnover frequency versus the ionising photon rate, from which we see a correlation between ν_{TO} and Q_{HI} , which has a probability $p(\tau) \leq 9.10 \times 10^{-6}$ of arising by chance. Given this correlation, we now assume that the sources which exhibit no turnover have not been searched to sufficiently low frequencies. We include these sources by assigning the lowest observed rest-frame frequency as the upper limit to this (e.g. Fanti et al. 1990). We also apply this to the 2nd order fit sources where the turnover frequency yielded by the fit is lower than the lowest observed rest-frame frequency (Fig. 11).

In order to incorporate the limits, we use the *Astronomy SURVival Analysis* (ASURV) package (Isobe et al. 1986) which adds these as censored data points, allowing a generalised non-parametric Kendall-tau test. Including these weakens the correlation ($p(\tau) \leq 2.3 \times 10^{-4}$)¹³, which may suggest, if $\nu_{\text{TO}} \propto Q_{\text{HI}}$, that the 1st order fit sources are not dominated by those which

¹² For the uncorrected ionising photon rates these are $p(t) = 0.992$ and $p(KS) = 0.045$.

¹³ For the uncorrected ionising photon rates this is $p(\tau) = 1.63 \times 10^{-4}$ (3.77 σ).

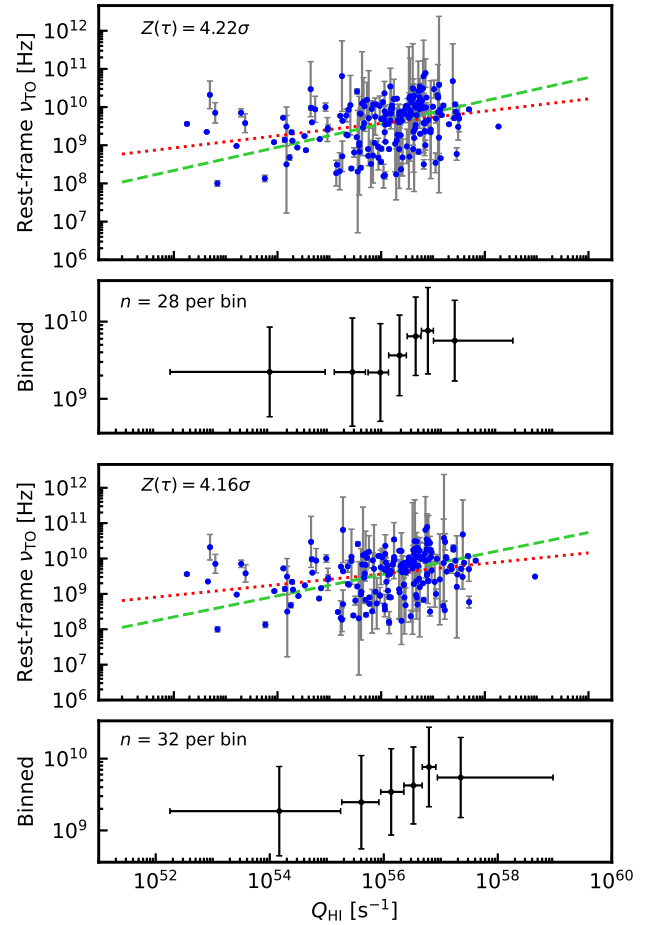


Figure 10. The rest-frame turnover frequency versus the measured (top) and corrected (bottom) ionising photon rate. In the top panel of each subplot the error bars show the uncertainty in the turnover frequency from the covariance of the 2nd order fit. The dotted (red) line shows the least-squares linear fit and the dashed (green) line the fit weighted by the 1σ uncertainty. In the bottom panel each bin contains the same number of sources, apart from the top bin which includes the strays (an additional two in the bottom plot only). These are centred on the mean values with the horizontal bar showing the range of the Q_{HI} bin and the vertical bar $\pm 1\sigma$ from the mean ν_{TO} .

have not been searched to low enough frequencies to detect the turnover. However, given the lower frequency ranges of the 1st order fit sources (Sect. 2.3.1), the detection of a turnover if the sampling were ample cannot be ruled out. Hence, it is also possible that the inclusion of these sources only acts to introduce noise.

2.4.2 Caveats

While we have found a strong correlation between the turnover frequency and the ionising photon rate, one should be aware of:

(i) For the one SDSS source which did match the low frequency catalogues, the lowest rest-frame frequency yielded by NED was 676 MHz, compared to 141 MHz from the low frequency data (Sect. 2.2.2). Thus, until observed and included in NED, allowing automated photometry scraping, it is reasonable to assume that many of the SDSS (1st order fit) sample have not been observed to sufficiently low frequencies.

(ii) The 1st order fit sources generally have sparser sampling

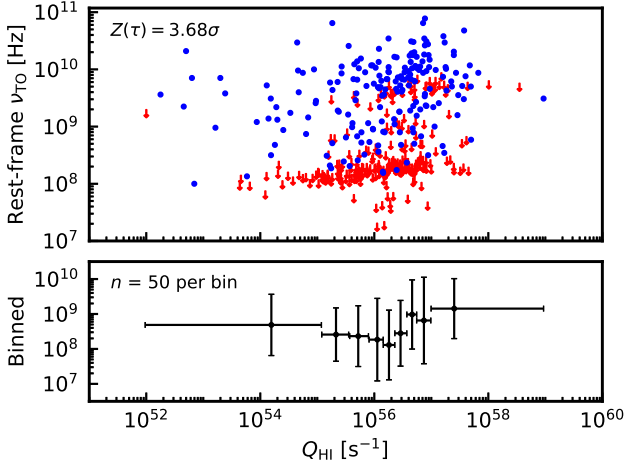


Figure 11. As the bottom plot of Fig. 10, but including the 1st order fit sources as upper limits to the turnover frequency (shown as downwards arrows). For clarity, the error bars are not shown in the top panel. In the bottom panel the limits are included in the binned values via the Kaplan & Meier (1958) estimator.

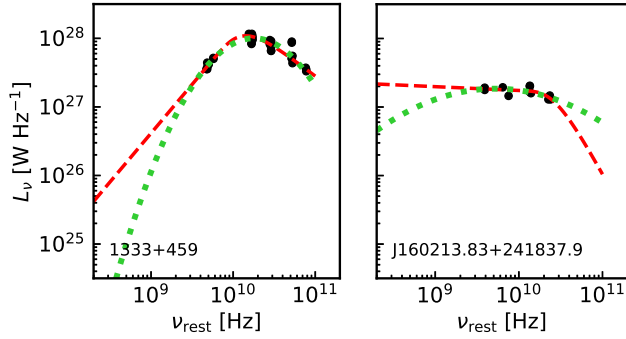


Figure 12. Left: Example of a low uncertainty in the turnover frequency, with $\log_{10} \nu_{\text{TO}} = 10.251 \pm 0.002$ from 25 photometry points. Right: Example of a high uncertainty, with $\log_{10} \nu_{\text{TO}} = 9.72 \pm 1.86$ from nine photometry points.

across the radio band (Sect. 2.3.1). So, until the power-law sources are sampled as comprehensively as those exhibiting a turnover, we cannot be certain that a potential turnover does not occur within the observed range.

(iii) As seen in Fig. 10, there is a large variation in the uncertainties in the turnover frequencies. Two examples, at either end of the range, are shown in Fig. 12. In a large enough sample we expect as many overestimates as underestimates, so that the biases introduced by these would be largely averaged out. Ideally, however, these should all be small and so, again, more comprehensive sampling of the radio band is required.

(iv) From the upper limits in Fig. 11, we see that the lowest observed frequency is correlated with the ionising photon rate, which is most likely driven by the redshift, where sources are observed to the same minimum frequency in a given survey, confirmed in Fig. 13. This is also evident in Gloudemans et al. (2023), where the high redshifts ($z = 5.6 - 6.6$) cause the low observed frequencies ($\gtrsim 0.1$ GHz) to be insensitive to turnover frequencies below ~ 1 GHz.

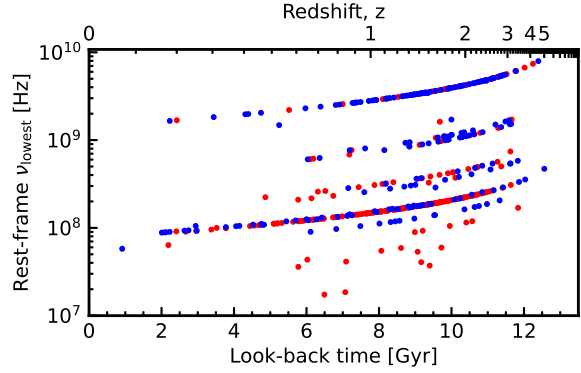


Figure 13. The rest-frame minimum observed frequencies versus redshift.

3 MODELLING THE $\nu_{\text{TO}} - Q_{\text{HI}}$ CORRELATION

3.1 Dependence of the turnover frequency on the photo-ionisation rate

We have found a correlation between the turnover frequency and the ionising photon rate (Fig. 10). Although this supports the hypothesis that there is a connection between the turnover frequency and ionising photon rate it is an empirical result. To explore the cause of the correlation we now examine the theoretical dependence between the turnover frequency, as caused by free-free absorption, and the number of photons available to ionise the neutral atomic gas.

For free-free radiation the absorption coefficient is

$$\kappa_\nu = \frac{\sqrt{2\pi}}{32} \frac{Z^2 e^6}{(4\pi\epsilon_0)^3} \frac{n_e^2}{c(m_e kT)^{3/2} \nu^2} \ln\left(\frac{3kT}{\nu h}\right), \quad (4)$$

where Z is the atomic number, e the electronic charge, n_e the electron density, k the Boltzmann constant, T the temperature, ϵ_0 the permittivity of free space, c the speed of light and m_e the electron mass.

For neutral hydrogen ($Z = 1$), this can be written as

$$\kappa_\nu = 0.0719 \left(\frac{n_e}{\nu}\right)^2 \frac{1}{T^{3/2}} \ln\left(\frac{3kT}{\nu h}\right), \quad (5)$$

per metre, where n_e is in cm^{-3} .

For a spherical H II region of radius r_{str} , at a luminosity distance D_L , the flux density is

$$S_\nu = (1 - e^{-\tau_\nu}) \pi \left(\frac{r_{\text{em}}}{D_L}\right)^2 B_\nu, \quad (6)$$

where $r_{\text{em}} = r_{\text{str}}$ for a sphere of constant density, the optical depth is $\tau_\nu = \int \kappa_\nu dr$ and B_ν is the specific brightness, which, in the Rayleigh-Jeans regime ($h\nu \ll kT$) is given by

$$B_\nu \approx \frac{2\nu^2}{c^2} kT. \quad (7)$$

In equilibrium, the rate of ionisation is balanced by the rate of recombination (Osterbrock 1989),

$$Q_{\text{HI}} \equiv \int_{\nu_{\text{ion}}}^{\infty} \frac{L_\nu}{h\nu} d\nu = 4\pi \int_0^{r_{\text{str}}} n_p n_e \alpha_A r^2 dr, \quad (8)$$

where n_p is the proton density and α_A the radiative recombination rate coefficient of hydrogen ($4.19 \times 10^{-13} \text{ cm}^3 \text{ s}^{-1}$ at the canonical $T = 10\,000$ K, Osterbrock & Ferland 2006).¹⁴

¹⁴ <http://amdpp.phys.strath.ac.uk/tamoc/DATA/RR/>

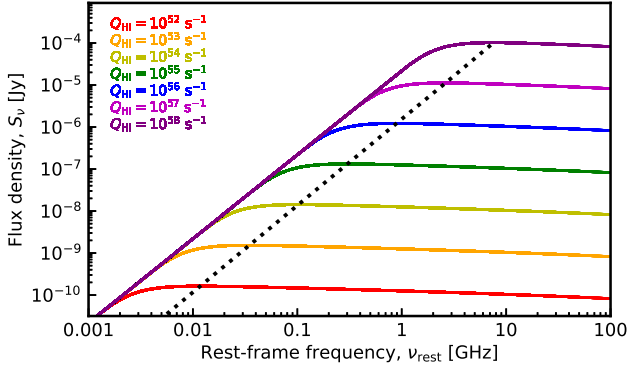


Figure 14. The radio SEDs for different photo-ionising rates for a $r_{\text{str}} = 1$ kpc sphere of $T = 10\,000$ K gas of constant density at $z = 1$. The flux density is for $r_{\text{em}} = r_{\text{str}}$. The densities which can be completely ionised within this sphere range from $n = 0.44 \text{ cm}^{-3}$ for $Q_{\text{HI}} = 1 \times 10^{52} \text{ s}^{-1}$ to $n = 440 \text{ cm}^{-3}$ for $Q_{\text{HI}} = 1 \times 10^{58} \text{ s}^{-1}$. The black dotted line shows the increase of ν_{TO} (as given by the maximum flux density) with Q_{HI} .

3.1.1 Constant density profile

From Equ. 8, the ionising photon rate required to completely ionise a neutral plasma ($n_p = n_e$) of constant density within a Strömgren sphere of radius r_{str} is

$$Q_{\text{HI}} = \frac{4}{3} \pi \alpha_A n_e^2 r_{\text{str}}^3. \quad (9)$$

For a range of ionising photon rates we use this to obtain the electron density, which we insert into Equ. 5, giving the absorption coefficient κ_ν . For a constant electron density through a path r_{str} , $\tau_\nu = \kappa_\nu r_{\text{str}}$ which, via Equ. 6, gives the variation in flux density with frequency (Fig. 14). From this, it is clear that for a given density, temperature and radius, the turnover frequency is correlated with the ionising photon rate, as is seen for the observational data (Sect. 2.4.1).

3.1.2 Exponential density profile

A more physically realistic model, especially on galactic scales, is an exponential decrease in gas density with distance from the nucleus of the galaxy (e.g. Baldwin 1982; Begeman et al. 1991). O’Dea & Baum (1997) use a distribution of the form $n = n_0 r^{-a}$, where $0 \lesssim a \lesssim 3$. However, this gives $n = 0$ at $r = 0$ and an infinite column density for $N_{\text{HI}} = \int_0^\infty n dr$. We therefore use the exponential sphere model, $n = n_0 e^{-r/R}$, which gives $N_{\text{HI}} = \int_0^\infty n dr = n_0 R$.

Using the Milky Way’s $N_{\text{HI}} = 3.3 \times 10^{22} \text{ cm}^{-2}$ and breaking the $n_0 R$ degeneracy via the gas mass (Curran & Whiting 2012)

$$M_{\text{gas}} = \frac{2\pi m_p n_0}{F} \int_0^\infty e^{-r/R} r^2 dr = \frac{4\pi m_p n_0 R^3}{F}, \quad (10)$$

where $F = 20$ is the Galactic flare factor (Kalberla & Kerp 2009), gives $M_{\text{gas}} = 5.3 \times 10^9 M_\odot$, $n_0 = 1.88 \text{ cm}^{-3}$ and $R = 5.66$ kpc for the Milky Way (Fig. 15). For the exponential sphere complete ionisation of the gas occurs when the ionising photon rate reaches (Curran & Whiting 2012)

$$Q_{\text{HI}} = \pi \alpha_A n_0^2 R^3. \quad (11)$$

Using Equ. 11 to obtain n_0 for a given R , where the gas is completely ionised (Fig. 16), gives the optical depth through the gas as

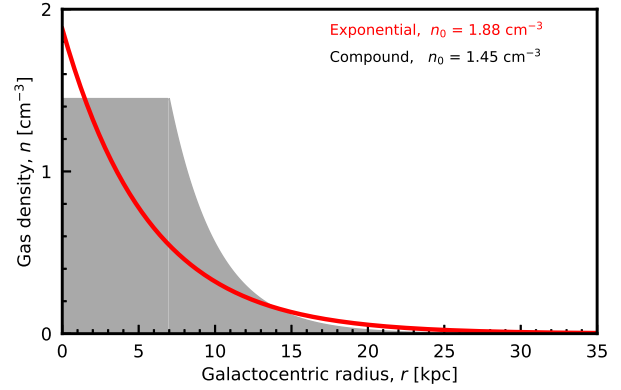


Figure 15. The gas density versus the galactocentric radius for the simple exponential (red) and compound (grey, see Sect. 3.1.3) models of the Milky Way.

(Equ. 5)

$$\tau_\nu = 0.0719 \left(\frac{1}{\nu}\right)^2 \frac{1}{T^{3/2}} \ln\left(\frac{3kT}{\nu h}\right) n_0^2 \int_0^\infty e^{-2r/R} dr.$$

Integrating this gives

$$\tau_\nu = \frac{0.0719}{2} \left(\frac{1}{\nu}\right)^2 \frac{1}{T^{3/2}} \ln\left(\frac{3kT}{\nu h}\right) n_0^2 R, \quad (12)$$

which, again via Equ. 6, gives the variation in flux density with frequency (Fig. 17, left). Like the constant density distribution, this exhibits an increase in the turnover frequency with ionising photon rate.

Although, unlike the constant density model, at large distances the path length is not required for the optical depth calculation, a value is required for the flux density (Equ. 6) and we have assumed that $r_{\text{em}} = 2.3R$ as the extent over which the emission can be detected. However, while the flux densities are not absolute, the turnover frequency is independent of the choice of r_{em} .

3.1.3 Constant and exponential density (compound) profile

For the Milky Way the gas distribution is a combination of both the constant and exponential profile (Kalberla & Kerp 2009);

$$n = \begin{cases} n_0, & r \leq r_0 \\ n_0 e^{-(r-r_0)/R}, & r > r_0, \end{cases}$$

where $n_0 = 1.45 \text{ cm}^{-3}$, $R = 3.15$ kpc and $r_0 = 7$ kpc (see Fig. 15). For this distribution complete ionisation of the gas occurs when the ionising photon rate is (Curran 2024)

$$Q_{\text{HI}} = \pi \alpha_A n_0^2 \left(\frac{4r_0^3}{3} + R [2r_0^2 + 2Rr_0 + R^2] \right). \quad (13)$$

Again, assuming that all of the gas is ionised, we use the electron density for a given ionising photon rate (Equ. 13) to calculate the optical depth through the gas

$$\tau_\nu = 0.0719 \left(\frac{1}{\nu}\right)^2 \frac{1}{T^{3/2}} \ln\left(\frac{3kT}{\nu h}\right) n_0^2 \left(\int_0^{r_0} dr + \int_{r_0}^\infty e^{-2r/R} dr \right),$$

which gives

$$\tau_\nu = \frac{0.0719}{2} \left(\frac{1}{\nu}\right)^2 \frac{1}{T^{3/2}} \ln\left(\frac{3kT}{\nu h}\right) n_0^2 \left(r_0 + \frac{R}{2} \right). \quad (14)$$

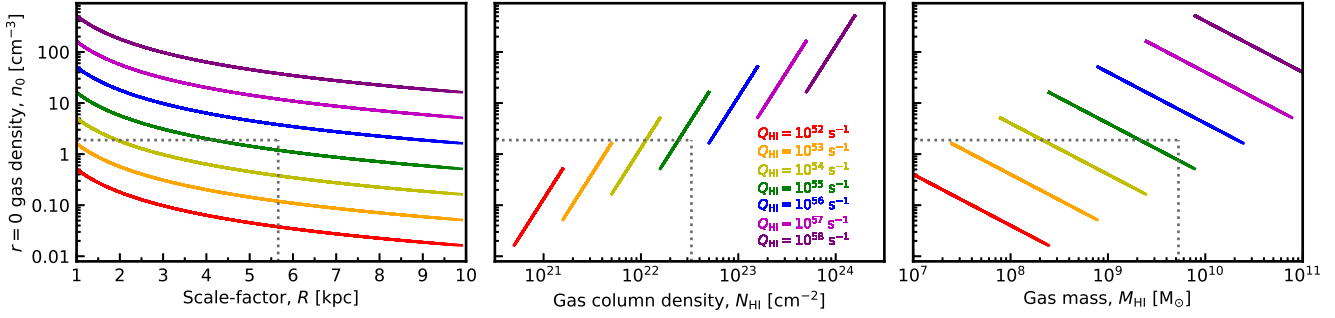


Figure 16. Left: The central gas density–scale-length degeneracy for complete ionisation of an exponential gas distribution as constrained by Equ. 11. Middle: The resulting column densities from $N_{\text{HI}} = n_0 R$. Right: The resulting gas masses, assuming the Galactic flare factor (Kalberla & Kerp 2009). The dotted line shows the values for the Galactic exponential distribution (Fig. 15), where all of the gas is ionised for $Q_{\text{HI}} > 2.5 \times 10^{55} \text{ s}^{-1}$.

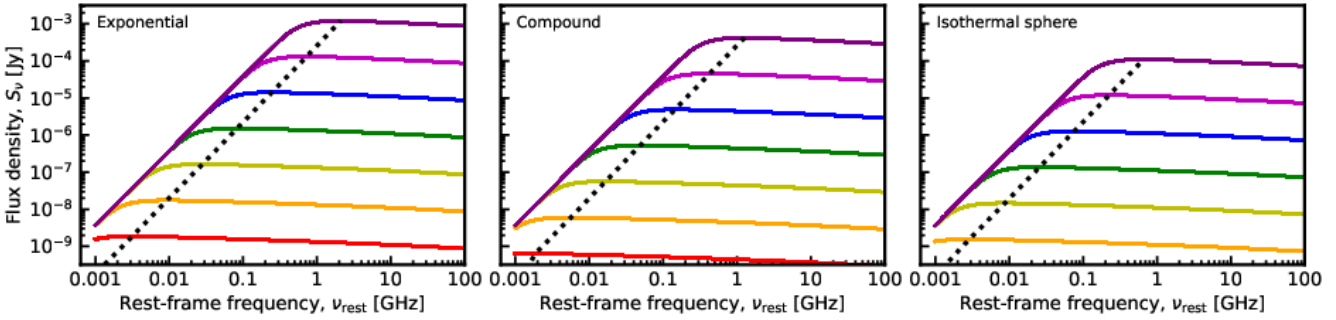


Figure 17. As Fig. 14. Left: For an exponential density profile. The central densities for which the gas can be completely ionised within this sphere range from $n_0 = 0.04 \text{ cm}^{-3}$ for $Q_{\text{HI}} = 10^{52} \text{ s}^{-1}$ to $n_0 = 37 \text{ cm}^{-3}$ for $Q_{\text{HI}} = 10^{58} \text{ s}^{-1}$. Middle: For a compound density profile, using the Galactic values of $r_0 = 7 \text{ kpc}$ and $R = 3.15 \text{ kpc}$. The central densities for which the gas can be completely ionised within this sphere range from $n_0 = 0.02 \text{ cm}^{-3}$ for $Q_{\text{HI}} = 1 \times 10^{52} \text{ s}^{-1}$ to $n_0 = 16.6 \text{ cm}^{-3}$ for $Q_{\text{HI}} = 1 \times 10^{58} \text{ s}^{-1}$. Right: For a spherical density profile. The central densities for which the gas can be completely ionised within this sphere range from $n_0 = 0.003 \text{ cm}^{-3}$ for $Q_{\text{HI}} = 10^{52} \text{ s}^{-1}$ to $n_0 = 33 \text{ cm}^{-3}$ for $Q_{\text{HI}} = 10^{58} \text{ s}^{-1}$.

This results in the frequency profiles shown in Fig. 17 (middle), where, again, we have assumed $r_{\text{em}} = 2.3R$ as the size of the emission region, although this does not affect the apparent $Q_{\text{HI}} - \nu_{\text{TO}}$ correlation.

3.1.4 Elliptical profiles

Since our sample comprises radio loud AGN, it is likely that most of the host galaxies are elliptical. These can be modelled via several similar density profiles, e.g. the Jaffe profile (Jaffe 1983), which models the distribution of light in a spherical galaxy as $n = n_0 (r_s/r)^2 / 4\pi (1 + r/r_s)^2$, where r_s is the radius which contains half the total emitted light. However, as seen in Fig. 18 this has an asymptotic density distribution, as does the NFW profile (Navarro et al. 1996), $n = n_0 (r_c/r) / (1 + r/r_c)^2$, where r_c is the radius of the halo core.

These can be avoided by employing the halo density distribution of an isothermal sphere, for example $n = n_0 / (1 + r/r_c)^2$ (Begeman et al. 1991) or equation 7 of Capelo et al. (2010),

$$n = n_0 \exp \left[-4\pi G \delta_c \rho_c r_s^2 \frac{\mu m_p}{kT} \left(1 - \frac{\ln(1 + r/r_s)}{r/r_s} \right) \right],$$

where G is the gravitational constant, ρ_c is the critical density of the Universe r_s is a scale radius, μ the mean molecular weight of the gas and m_p the proton mass. We select this, the simplest model, cf. the polytropic and stellar models, to limit the number of free parameters. Using the column density of the Milky Way at $r = 35 \text{ kpc}$ ($N_{\text{HI}} = 3.25 \times 10^{22} \text{ cm}^{-2}$) to constrain the characteristic density gives $\delta_c = 2370$ for $T = 10000 \text{ K}$ and $r_s = R$.

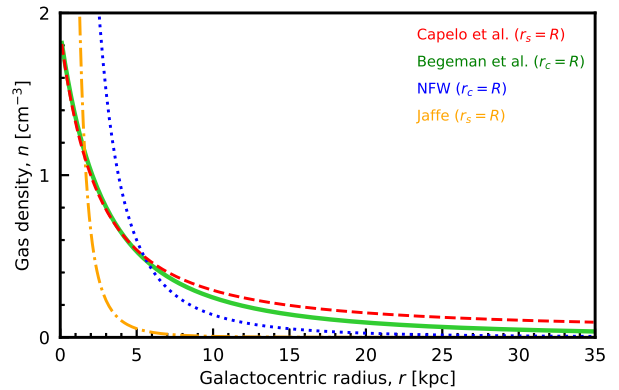


Figure 18. The gas density versus the galactocentric radius for the Jaffe (1983), Begeman et al. (1991), Navarro et al. (1996) and Capelo et al. (2010) models. In all cases we use the scale-length and central density of the simple exponential model of the of the Milky Way (Fig. 15).

Given its relative simplicity, while yielding a similar density profile to that of Capelo et al. (2010), we use the profile of Begeman et al., for which complete ionisation of the gas occurs when

$$Q_{\text{HI}} = \frac{4}{3} \pi \alpha_A n_e^2 r_c^3.$$

Proceeding as above, the optical depth through the completely

Table 1. The turnover frequencies predicted from the different gas models for different ionising photons rates. The last column is for the isothermal sphere in Sect. 3.1.4.

$Q_{\text{HI}} [\text{s}^{-1}]$	Gas density model			
	Constant	Exponential	Compound	Iso. Sphere
10^{52}	11 MHz	1.9 MHz	8.5 MHz	1.0 MHz
10^{53}	35 MHz	5.6 MHz	25 MHz	2.9 MHz
10^{54}	100 MHz	16 MHz	74 MHz	8.7 MHz
10^{55}	300 MHz	49 MHz	220 MHz	26 MHz
10^{56}	0.89 GHz	140 MHz	0.65 GHz	76 MHz
10^{57}	2.6 GHz	0.43 GHz	1.9 GHz	0.22 GHz
10^{58}	8.8 GHz	1.3 GHz	5.5 GHz	0.66 GHz

ionised gas is

$$\tau_\nu = 0.0719 \left(\frac{1}{\nu}\right)^2 \frac{1}{T^{3/2}} \ln\left(\frac{3kT}{\nu h}\right) n_0^2 \int_0^\infty \frac{dr}{(1+r/r_c)^4},$$

giving

$$\tau_\nu = \frac{0.0719}{2} \left(\frac{1}{\nu}\right)^2 \frac{1}{T^{3/2}} \ln\left(\frac{3kT}{\nu h}\right) n_0^2 \frac{r_c}{3}. \quad (15)$$

which has a similar form to the exponential density (Equ. 12) and frequency (Fig. 17, right) profiles.

3.1.5 Summary

For all of the above models $\nu_{\text{TO}} \propto Q_{\text{HI}}^{0.97}$, although there is some variation in the constant of proportionality and each model therefore predicts quite different values for the turnover frequency, which can vary by up to an order of magnitude for a given ionising rate (Table 1). Only where there is a constant density component, will we see a turnover at $\nu_{\text{TO}} \sim 1$ GHz for $Q_{\text{HI}} \sim 10^{56} \text{ s}^{-1}$ (sufficient to ionise all of the gas in a large spiral). For the exponential and spherical models it appears that $Q_{\text{HI}} \gtrsim 10^{58} \text{ s}^{-1}$ is required for $\nu_{\text{TO}} \sim 1$ GHz, which is consistent with the hypothesis that sources with no turnover are not subject to complete ionisation.

3.2 The turnover frequency of J0002+2550

Equipped with the expected value of the turnover frequency for a given photo-ionisation rate, we can estimate the turnover for J0002+2550 (Sect. 2.2.1). At $z = 5.80$, the luminosity distance to the source is $D_L = 56\,900$ Mpc and the finest beam size of $3.4''$, in which the source is unresolved (Gloude-mans et al. 2023), gives $r_{\text{em}} \lesssim 10$ kpc for the low frequency emission.

Again, assuming complete ionisation by the observed $Q_{\text{HI}} = 9.3 \times 10^{54} \text{ s}^{-1}$ (Sect. 2.2.1), in Fig. 19 we show the expected radio SED for various scale-lengths from which it is apparent that, for a scale-length of $R \gtrsim 0.1$ kpc, the turnover frequency is $\lesssim 1$ GHz. Although consistent with the absence of a turnover at $\nu_{\text{TO}} \gtrsim 1$ GHz, our simple free-free radiation model (which forces $\alpha_{\text{thick}} \approx 2$ and $\alpha_{\text{thin}} \approx -0.1$) does not trace the steep spectral index of the optically thin portion of the Gloude-mans et al. spectrum (where $\alpha_{\text{thin}} \approx -1.6$), which they attribute to the ionised medium producing synchrotron emission in addition to a spectral break caused by ageing electrons.

We note that the predicted flux density approaches the observed ~ 1 mJy at $\nu_{\text{rest}} \sim 1$ GHz, for a scale length of $R \sim 100$ pc. This is about an order of magnitude lower than that of

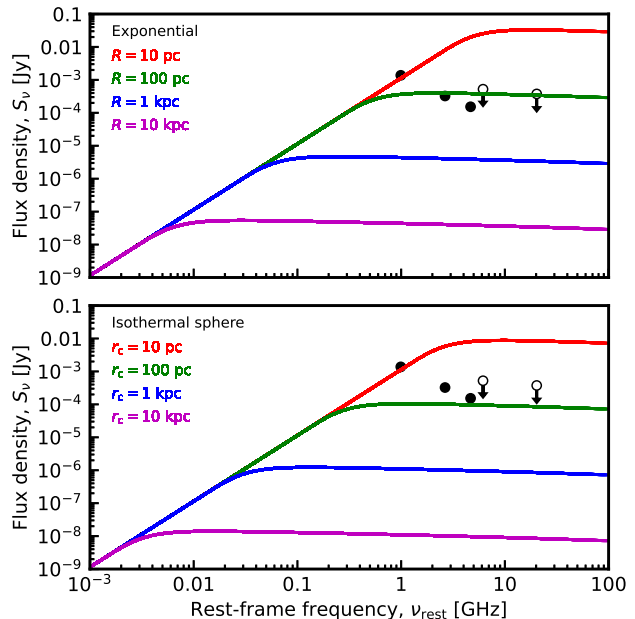


Figure 19. The radio SED from an $r_{\text{em}} = 10$ kpc H II region at $z = 5.80$ due to a $Q_{\text{HI}} = 1.0 \times 10^{55} \text{ s}^{-1}$ ionising rate for different scale-lengths of the gas density distribution. The points and upper limits show the photometry from Gloude-mans et al. (2023).

the Galaxy but, due to hierarchical build-up, we expect smaller galaxies (Baker et al. 2000; Lanfranchi & Friaça 2003) and, thus, smaller scale-lengths at high redshift. However, we have set the extent of the emission to the minor axis of the smallest beam in which the source is unresolved, and so there is some wriggle room in the absolute flux measurements.

Correcting the UV spectral index for J0002+2550 gives $\alpha_{\text{UV}} = -9.4$, which results in an ionising photon rate of $Q_{\text{HI}} = 1.0 \times 10^{55} \text{ s}^{-1}$, which changes little from the uncorrected value. From Table 1, we see that the exponential and spherical gas density profiles allow for no turnover at $\nu \gtrsim 1$ GHz for relatively high ionising rates ($Q_{\text{HI}} \lesssim 10^{58} \text{ s}^{-1}$), whereas the constant density model precludes this at $Q_{\text{HI}} \gtrsim 10^{56} \text{ s}^{-1}$. Unfortunately, the other targets of Gloude-mans et al. have insufficient rest-frame UV photometry to see if such steep UV spectra apply to the sample as a whole (see Appendix C). As it is, this source is consistent with a low level of ionisation causing shifting the turnover frequency to below the minimum observed value, but with the caveat that the photometry correction for intervening absorption is statistical only.

3.3 Turnover frequency and size

3.3.1 Observations

As stated in Sect. 1, the turnover frequency is anti-correlated with the projected linear size, which is clearly evident in the O’Dea & Baum (1997) data (Fig. 20).¹⁵ On average, the turnover frequencies we derive are slightly lower than those of O’Dea & Baum, which could be due to the recent increase in the availability of low frequency data (see Appendix B). Out of the 66 sources with a measured linear size, 38 exhibit a turnover,

¹⁵ ℓ is calculated using updated spectroscopic redshifts and cosmological parameters (Planck Collaboration et al. 2020).

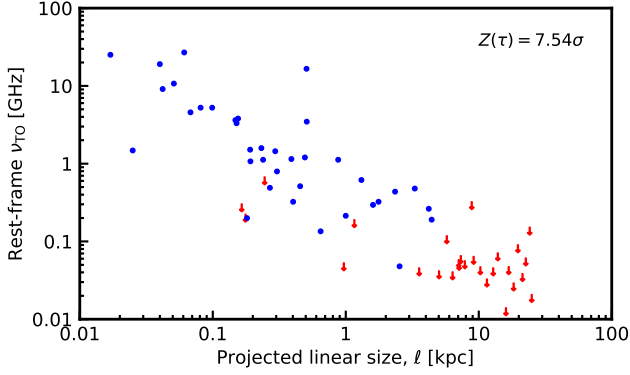


Figure 20. The turnover frequencies versus the projected linear size for the sample of O’Dea & Baum (1997).

27 are flagged as upper limits, since the fit gives a turnover below the lowest observed frequency, and one has an inverted spectrum (FBQS J133037.6+250910). Including the limits, and excluding J1330+2509, we obtain $p(\tau) = 4.56 \times 10^{-14}$ for the correlation, which is similar to that using the values of O’Dea & Baum directly, where there are no limits.¹⁶

3.3.2 Model

If the extent of the radio emission scales with R , the anti-correlation between turnover frequency and size is evident from our model. Furthermore, for an ionising photon rate of $Q_{\text{H I}} \sim 10^{55} \text{ s}^{-1}$ (J0002+2550, Fig. 19) and $R \sim \ell$, the model is in agreement with the observations (Sect. 1); that is, $\nu_{\text{TO}} \sim 0.4 - 5 \text{ GHz}$ for $R \lesssim 1 \text{ kpc}$ (HFPs/GPSs) and $\nu_{\text{TO}} \lesssim 0.5 \text{ GHz}$ for $R \gtrsim 10 \text{ kpc}$ (CSSs).

In order to generalise this, we need to break the degeneracy between n_0 and R in Equ. 12. For this we use the exponential model for which we can use the fact that, for a given mass, the product $n_0 R^3$ is constant (Equ. 10).¹⁷ From a low-redshift survey of 21-cm emission from the 1000 HI brightest galaxies in the southern sky, Koribalski et al. (2004) find a range of $M_{\text{gas}} \sim 10^7 - 10^{11} M_{\odot}$, with a median of $M_{\text{gas}} = 2.9 \times 10^9 M_{\odot}$. Using these masses and assuming the Galactic flare factor, for a given scale-length we determine n_0 , which is then used in Eqs. 12 and 6 to produce an SED (as for Fig. 19), from which we obtain the turnover frequency.¹⁸

The results are shown in Fig. 21, where we see the predictions overlap the observations of O’Dea & Baum (1997) for the range of gas masses expected (assuming $R = \ell$). We also note that the median gas mass of $M_{\text{gas}} = 2.9 \times 10^9 M_{\odot}$ passes close to the middle of the distribution of the observed data. This is also closely aligned with the two models of O’Dea & Baum, which are based on synchrotron self-absorption models. Thus, for a gas scale-length close to the radio source size, our simple free-free model can reproduce the observed $\nu_{\text{TO}}-\ell$ relationship.

Lastly, we note that, while we are considering the ionisation of the large-scale gas, the material causing the turnover in the radio SED may be mainly located within the central $\sim 1 \text{ kpc}$

¹⁶ $p(\tau) = 1.58 \times 10^{-13}$ (7.38 σ).

¹⁷ For the spherical model (Sect. 3.1.4), $M_{\text{gas}} = 2\pi m_p n_0 \int_0^\infty r^2 dr / (1 + r/r_c^2) = 4\pi n_0 r_c^3 [1 + \frac{r}{r_c} - \frac{r_c}{r_c+r} - 2 \ln(r_c + r) + 2 \ln(r_c)]_0^\infty$.

¹⁸ In Equ. 6, r_{em} and D_L are only required to obtain the absolute flux density.

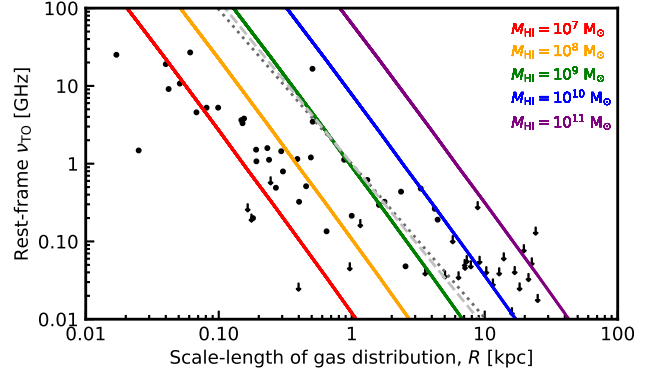


Figure 21. The turnover frequency at various total gas masses for completely ionised gas of scale-length R . The markers show the data of O’Dea & Baum (Fig. 20), assuming $\ell = R$ and the dotted and dashed lines their models 1 & 2, respectively.

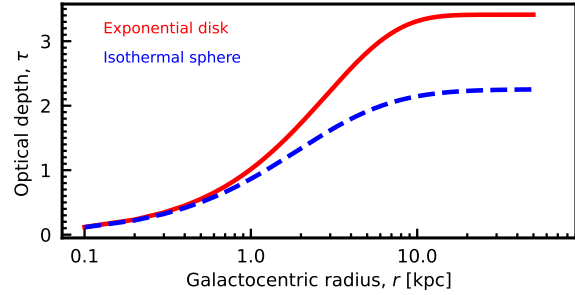


Figure 22. The optical depth of the 100 MHz absorption versus the distance traversed through the gas for the $R = 5.66 \text{ kpc}$ and $n_0 = 1.88 \text{ cm}^{-3}$ exponential density profile (Sect. 3.1.2) and the $r_c = 5.66 \text{ kpc}$ and $n_0 = 1.88 \text{ cm}^{-3}$ spherical density profile (Sect. 3.1.4).

(e.g. Dallacasa et al. 2000; Callingham et al. 2015; Maccagni et al. 2018). However, for the exponential and isothermal sphere models of the gas density, we see that at 100 MHz the absorption is already optically thick within this region (Fig. 22).

3.4 Ionising photon rates of the O’Dea & Baum sample

Of the O’Dea & Baum sample, only 11 sources have sufficient rest-frame photometry to yield an ionising photon rate, comprising five with a turnover within the sampled frequency range and six without. As seen from Fig. 23, five detections and six limits are insufficient to yield a convincing correlation ($p(\tau) = 0.085$), although one is suggested by the binning.

4 DISCUSSION AND CONCLUSIONS

It has long been known that the turnover frequency in the SEDs of extragalactic radio sources is anti-correlated with the projected size of the emission. If the profile of the radio SED is dominated by free-free absorption we may expect the turnover frequency, ν_{TO} , to be related to the rate of ionising photons emitted by the AGN. Thus, we suggest that radio sources which do not exhibit a turnover have low ionising photon rates, causing the turnover to be below the minimum observed frequency.

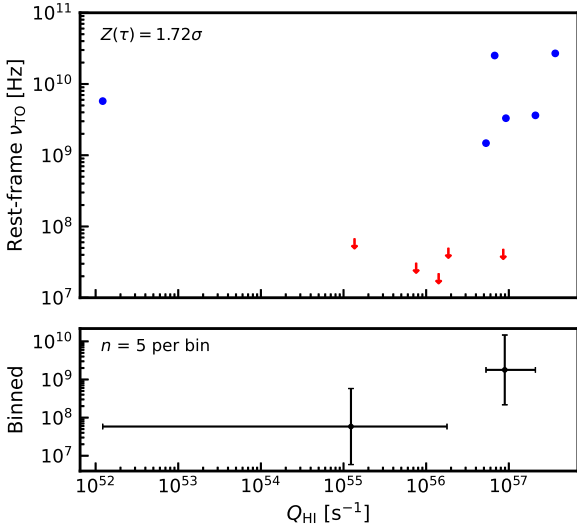


Figure 23. The turnover frequency versus the ionising photon rate for the sample of O’Dea & Baum (1997).

To test this, we initially examined the observational data, mining all of the radio, IR, optical and UV photometry, in order to obtain the turnover frequency and ionising photon rate:

- For the sample of Gloude-mans et al. (2023), where only one of the nine high redshift sources shows any indication of a turnover: Sufficient rest-frame UV photometry was available for only one source, J0002+2550. This was found to have a relatively low ionising photon rate of $Q_{\text{HI}} \sim 10^{55} \text{ s}^{-1}$, which is consistent with a low turnover frequency.
- For a larger sample, optically selected in order to increase the number of sources with comprehensive UV photometry:

- For the sources which exhibit a turnover in their radio SED, we find a correlation between ν_{TO} and Q_{HI} , significant at $\approx 4.2\sigma$.
- By assuming that the radio sources fit by a power-law have their turnover frequencies below the minimum observed, the significance reduces to $\approx 3.7\sigma$. However, there is strong evidence that the power-law sources are not as comprehensively sampled in the radio band than those exhibiting a turnover, and, if these do have a putative undetected peak in the spectrum, including these adds noise to the data. Thus, more complete sampling in the radio band for the power-law sources is required.

While compelling, the correlation between the turnover frequency and the ionising photon rate is an empirical result and so, to provide a physical justification, we produced a model relating ν_{TO} to Q_{HI} , via the electron density. This is done by assuming purely free-free radiation from a completely ionised galactic disk/sphere. From this we find;

- For gas of a constant density, an exponential density profile, a combination of both (as per the Milky Way) and a spherical density profile, that the turnover frequency is correlated with ionising photon rate, which must exceed that to ionise all of the gas in a large spiral ($Q_{\text{HI}} \gtrsim 10^{56} \text{ s}^{-1}$) in order to exhibit $\nu_{\text{TO}} \gtrsim 1 \text{ GHz}$. This supports the hypothesis that sources with low ionising photon rates ($Q_{\text{HI}} \ll 10^{56} \text{ s}^{-1}$) have their turnover frequencies below the minimum observed ($\nu_{\text{TO}} \ll 1 \text{ GHz}$)
- That the exponential and spherical density models can fit the SED of J0002+2550 for $R \gtrsim 100 \text{ pc}$, suggesting that the turnover

frequency is indeed below the lowest observed rest-frame frequency of 1 GHz.

- For a given mass of neutral gas, and using the scale-length as a proxy for the projected linear size, the dependence of turnover frequency on the scale-length of the exponential gas distribution closely traces the observational data and the synchrotron self-absorption model.

The model, which relies solely on ionisation of the atomic gas by the AGN, is considerably simpler than the synchrotron self-absorption models (Bicknell et al. 1997; O’Dea & Baum 1997), which have to assume a large number of magnetic field reversals to keep net polarisation at the low values which are observed.

However, given the sparseness of the radio data, when prioritising sources with measured UV luminosities, we cannot reliably determine spectral indices below and above the turnover. A further caveat is we assume that the gas is completely ionised, although the fact that all of the distributions tested give the same dependence $\nu_{\text{TO}} \propto Q_{\text{HI}}^{0.97}$ may suggest that the model remains valid over a region of ionisation enclosed within an envelope of neutral gas. We also assume that the scale-length of the gas distribution is proportional to the extent the emission. This is a reasonable assumption and only affects the flux density of the modelled source and not the turnover frequency. Interestingly, setting the scale-length $R = \ell$ does reproduce the $\nu_{\text{TO}}-\ell$ synchrotron self-absorption models (O’Dea & Baum 1997) for the median gas mass ($M_{\text{gas}} \sim 10^9 M_{\odot}$).

Future wide-field spectroscopy of radio sources, including those of the low frequency sample, e.g with WEAVE (Dalton et al. 2012; Smith et al. 2016), will allow us to determine many more ionising photon rates for the sources which have been observed to considerably lower frequencies than the SDSS sample. These will prove invaluable in determining whether the power-law sources have simply not been observed to sufficiently low frequencies, as posited here. With a large number of sources probed to very low frequencies, we may also be able to constrain which gas distribution best follows the model and perhaps yield an estimate of the ionising photon rate in the absence of observed frame UV-optical-IR photometry. A strong anti-correlation between the abundance of cool neutral gas and the ionising photon rate has been long established (Curran et al. 2008; Curran 2024) and, in the absence of observationally expensive follow-up UV photometry, it will be interesting to see if the turnover frequency is also anti-correlated with the detection of HI absorption from ongoing and future surveys with the SKA and its pathfinders, e.g. the *First Large Absorption Survey in HI* (FLASH, Allison et al. 2022).

DATA AVAILABILITY

Data available on request and the NED photometry data are included in the online versions.

ACKNOWLEDGEMENTS

I would like to thank the anonymous referee and the scientific editors, Tim Pearson, for their helpful and constructive comments which helped improve the manuscript. This research has made use of the NASA/IPAC Extragalactic Database (NED) which is operated by the Jet Propulsion Laboratory, California Institute of Technology, under contract with the National Aeronautics and Space

Administration and NASA's Astrophysics Data System Bibliographic Service. This research has also made use of NASA's Astrophysics Data System Bibliographic Service and ASURV Rev 1.2 (Lavalley et al. 1992), which implements the methods presented in Isobe et al. (1986).

REFERENCES

- Alam S. et al., 2015, *ApJS*, 219, 12
- Allison J. R. et al., 2022, *PASA*, 39, e010
- An T., Baan W. A., 2012, *ApJ*, 760, 77
- Bañados E. et al., 2014, *AJ*, 148, 14
- Baker A. C., Mathlin G. P., Churches D. K., Edmunds M. G., 2000, in *Star Formation from the Small to the Large Scale*, Vol.45 of ESA SP, Favata F., Kaas A., Wilson A., eds., ESA Special Publication, Noordwijk, p. 21
- Baldwin J. E., 1982, in *Extragalactic Radio Sources*, Heeschen D. S., Wade C. M., eds., Vol. 97, pp. 21–24
- Barger A. J., Cowie L. L., 2010, *ApJ*, 718, 1235
- Begelman M. C., 1999, in *The Most Distant Radio Galaxies*, Röttgering H. J. A., Best P. N., Lehnert M. D., eds., p. 173
- Begeman K. G., Broeils A. H., Sanders R. H., 1991, *MNRAS*, 249, 523
- Bicknell G. V., Dopita M. A., O'Dea C. P. O., 1997, *ApJ*, 485, 112
- Callingham J. R. et al., 2017, *ApJ*, 836, 174
- Callingham J. R. et al., 2015, *ApJ*, 809, 168
- Capelo P. R., Natarajan P., Coppi P. S., 2010, *MNRAS*, 407, 1148
- Curran S. J., 2024, *PASA*, 41, 7
- Curran S. J., Hunstead R. W., Johnston H. M., Whiting M. T., Sadler E. M., Allison J. R., Athreya R., 2019, *MNRAS*, 484, 1182
- Curran S. J., Moss J. P., Perrott Y. C., 2021, *MNRAS*, 503, 2639
- Curran S. J., Whiting M. T., 2012, *ApJ*, 759, 117
- Curran S. J., Whiting M. T., Sadler E. M., Bignell C., 2013, *MNRAS*, 428, 2053
- Curran S. J., Whiting M. T., Wiklind T., Webb J. K., Murphy M. T., Purcell C. R., 2008, *MNRAS*, 391, 765
- Dallacasa D., Stanghellini C., Centonza M., Fanti R., 2000, *A&A*, 363, 887
- Dalton G. et al., 2012, in *Society of Photo-Optical Instrumentation Engineers (SPIE) Conference Series*, Vol. 8446, *Ground-based and Airborne Instrumentation for Astronomy IV*, McLean I. S., Ramsay S. K., Takami H., eds., p. 84460P
- Fanti C., Fanti R., Dallacasa D., Schilizzi R. T., Spencer R. E., Stanghellini C., 1995, *A&A*, 302, 317
- Fanti R., Fanti C., Schilizzi R. T., Spencer R. E., Nan Rendong, Parma P., van Breugel W. J. M., Venturi T., 1990, *A&A*, 231, 333
- Gloude-mans A. J. et al., 2022, *A&A*, 668, A27
- Gloude-mans A. J. et al., 2023, *A&A*, 678, A128
- Isobe T., Feigelson E., Nelson P., 1986, *ApJ*, 306, 490
- Jaffe W., 1983, *MNRAS*, 202, 995
- Janknecht E., Baade R., Reimers D., 2002, *A&A*, 391, L11
- Kalberla P. M. W., Kerp J., 2009, *Ann. Rev. Astr. Ap.*, 47, 27
- Kaplan E. L., Meier P., 1958, *J. Amer. Statist. Assoc.*, 53, 457
- Kato T., Tabara H., Inoue M., Aizu K., 1987, *Nat*, 329, 223
- Keim M. A., Callingham J. R., Röttgering H. J. A., 2019, *A&A*, 628, A56
- Koribalski B. S. et al., 2004, *AJ*, 128, 16
- Lanfranchi G. A., Friaça A. C. S., 2003, *MNRAS*, 343, 481
- Lavalley M. P., Isobe T., Feigelson E. D., 1992, in *BAAS*, Vol. 24, pp. 839–840
- Maccagni F. M., Morganti R., Oosterloo T. A., Oonk J. B. R., Emonts B. H. C., 2018, *A&A*, 614, A42
- Marr J. M., Perry T. M., Read J., Taylor G. B., Morris A. O., 2014, *ApJ*, 780, 178
- Mo H., van den Bosch F. C., White S., 2010, *Galaxy Formation and Evolution*. Cambridge University Press, Cambridge
- Navarro J. F., Frenk C. S., White S. D. M., 1996, *ApJ*, 462, 563
- O'Dea C. P., 1998, *PASP*, 110, 493
- O'Dea C. P., Baum S. A., 1997, *AJ*, 113, 148
- O'Dea C. P., Baum S. A., Stanghellini C., 1991, *ApJ*, 380, 66
- O'Dea C. P., Saikia D. J., 2021, *ARA&A*, 29, 3
- Osterbrock D. E., 1989, *Astrophysics of Gaseous Nebulae and Active Galactic Nuclei*. University Science Books, Mill Valley, California
- Osterbrock D. E., Ferland G. J., 2006, *Astrophysics of Gaseous Nebulae and Active Galactic Nuclei*. University Science Books, Sausalito, California
- Planck Collaboration et al., 2020, *A&A*, 641, A6
- Readhead A. C. S., Taylor G. B., Pearson T. J., Wilkinson P. N., 1996, *ApJ*, 460, 634
- Shull J. M., Stevans M., Danforth C. W., 2012, *ApJ*, 752, 162
- Skrutskie M. F. et al., 2006, *AJ*, 131, 1163
- Slob M. M., Callingham J. R., Röttgering H. J. A., Williams W. L., Duncan K. J., de Gasperin F., Hardcastle M. J., Miley G. K., 2022, *A&A*, 668, A186
- Smith D. J. B. et al., 2016, in *SF2A-2016: Proceedings of the Annual meeting of the French Society of Astronomy and Astrophysics*, Reylé C., Richard J., Cambrésy L., Deleuil M., Pécontal E., Tresse L., Vauglin I., eds., pp. 271–280
- Snellen I. A. G., Schilizzi R. T., de Bruyn A. G., Miley G. K., Rengelink R. B., Roettgering H. J., Bremer M. N., 1998, *A&AS*, 131, 435
- Stanghellini C., O'Dea C. P., Dallacasa D., Baum S. A., Fanti R., Fanti C., 1998, *A&AS*, 131, 303
- Telfer R. C., Zheng W., Kriss G. A., Davidsen A. F., 2002, *ApJ*, 565, 773
- Tingay S. J. et al., 2015, *AJ*, 149, 74
- Wright E. L. et al., 2010, *AJ*, 140, 1868

APPENDICES

A: NED photometry

The NED photometry for each of our samples are included online in the files `SDSS_NED-fluxes.txt` (the SDSS sample), `G23_NED-fluxes.txt` (the Gloude-mans et al. sample) and `Low-sample_NED-fluxes.txt`. These are in the format

No	NED1	NED2	z	log10(Freq)	log10(Flux)
1	SDSS	J205212.82+001137.4	0.6864645	15.29	-4.82
1	SDSS	J205212.82+001137.4	0.6864645	15.29	-4.92
1	SDSS	J205212.82+001137.4	0.6864645	15.29	-4.83
1	SDSS	J205212.82+001137.4	0.6864645	15.13	-4.67
1	SDSS	J205212.82+001137.4	0.6864645	15.11	-4.72

where the source number is followed by the NED name, the redshift and \log_{10} of the observed frequency (Hz) and flux (Jy). Note that `Low-sample_NED-fluxes.txt` has an additional field designating the reference for the source: C17 – Callingham et al. (2017), G22 – Gloude-mans et al. (2022), S22 – Slob et al. (2022).

B: The O’Dea & Baum sample

In Fig. 24 we show the SEDs of O’Dea & Baum (1997) with our fits to the UV (Sect. 2.1) and radio (Sect. 2.1) photometry.

In Fig. 25 we show the turnover frequencies obtained from our fits compared to those of O’Dea & Baum (1997).

C: The Gloude-mans et al. sample

In addition to Fig. 2, we show in Fig. 26 the photometry scraped from NED, WISE, 2MASS and GALEX for the sources of Gloude-mans et al. (2023). Note that for the remaining four sources no photometric data were available.

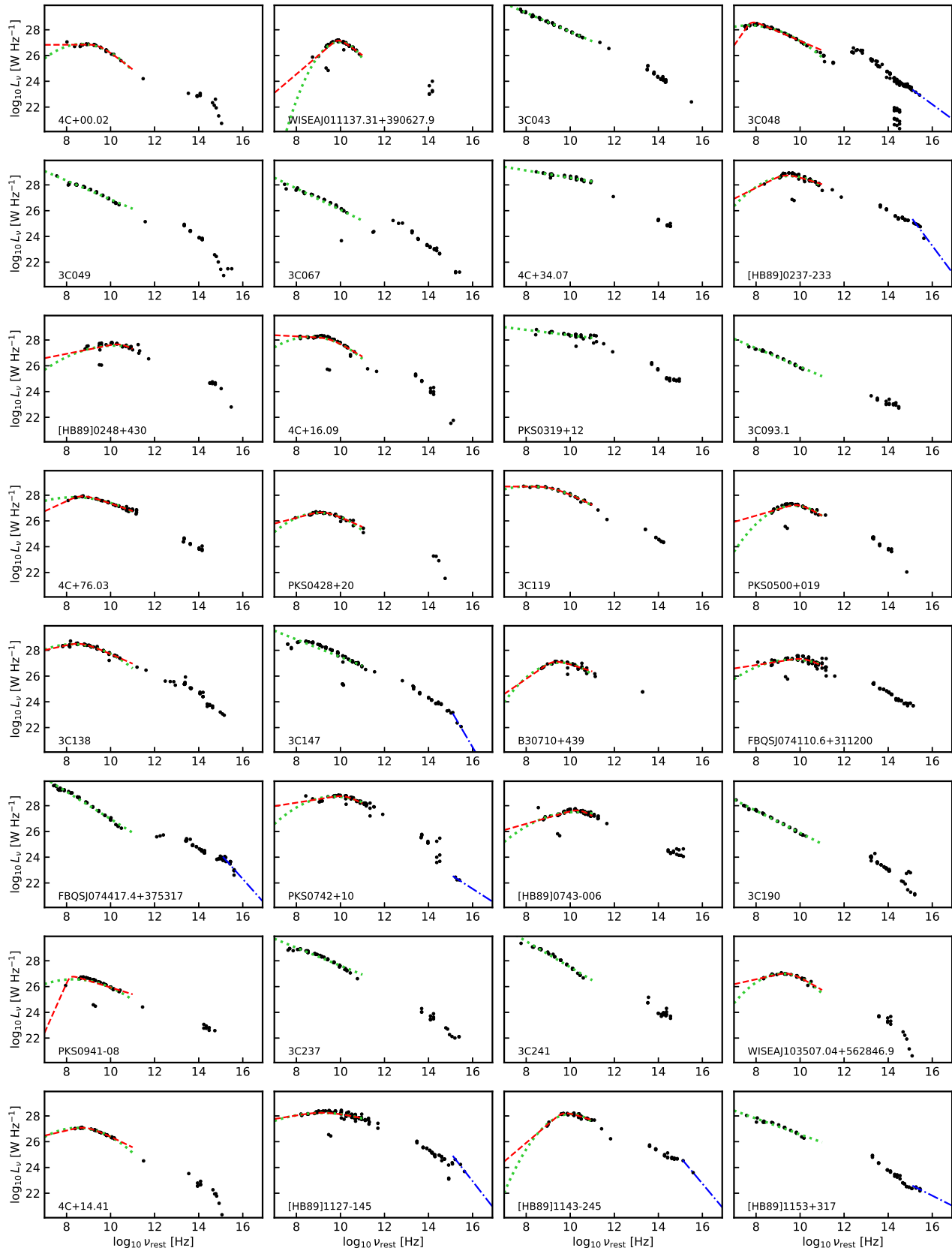
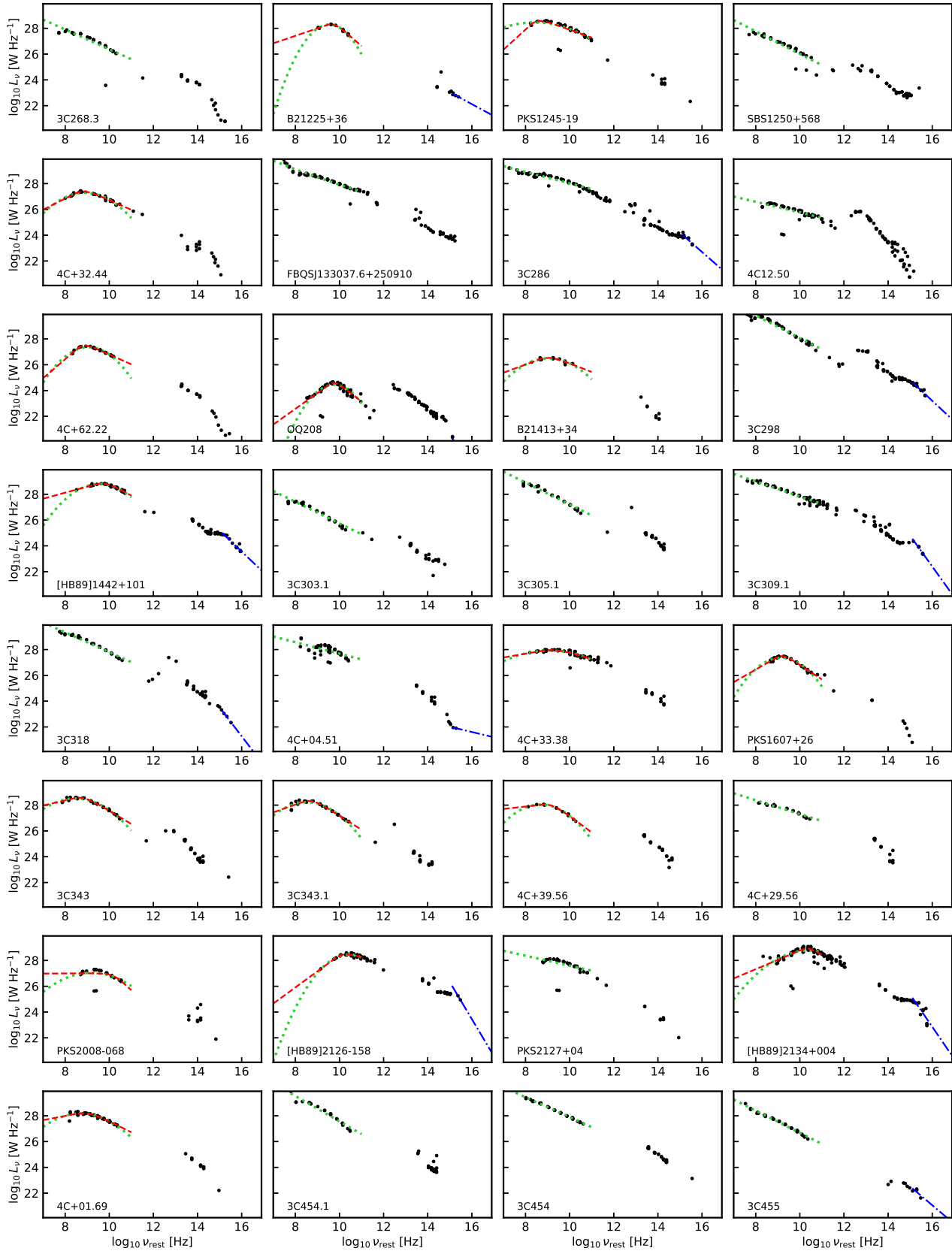


Figure 24. The SEDs and fits to the O’Dea & Baum sample. The curves show the fits to the radio data (polynomial – dotted, GPS-fit – dashed) and the line the power-law fit to the UV data.


 Figure 24. *Continued*

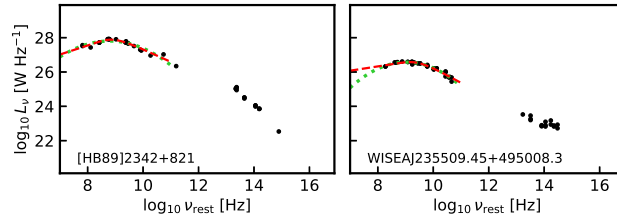


Figure 24. *Continued*

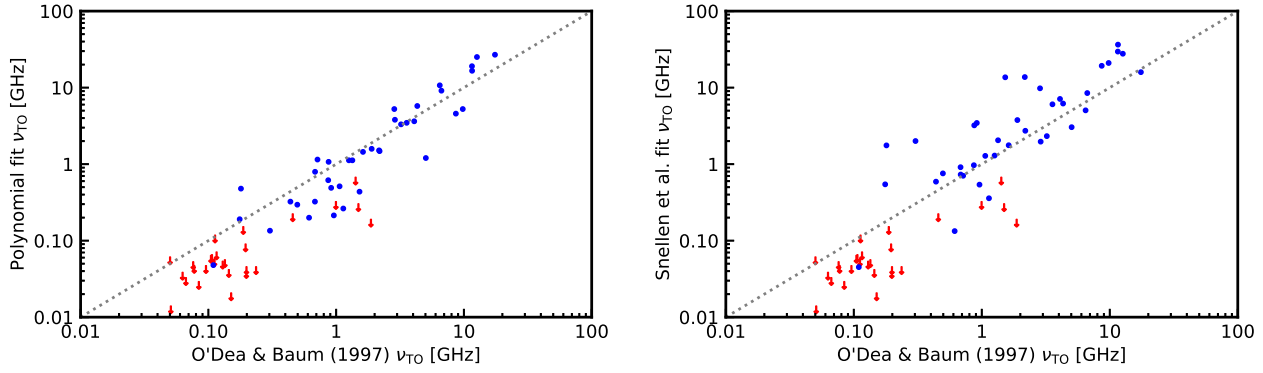


Figure 25. Our derived turnover frequencies compared to those of O’Dea & Baum. The arrows show the upper limits and the dotted line where these are equal ($\Delta \log_{10} \nu_{\text{TO}} [\text{GHz}] = 0$). Left: For the polynomial radio SED fit ($\Delta \log_{10} \nu_{\text{TO}} [\text{GHz}] = -0.098$, excluding the limits). Right: For the Snellen et al. (1998) radio SED fit ($\Delta \log_{10} \nu_{\text{TO}} [\text{GHz}] = 0.188$, excluding the limits), see Sect. 2.1.

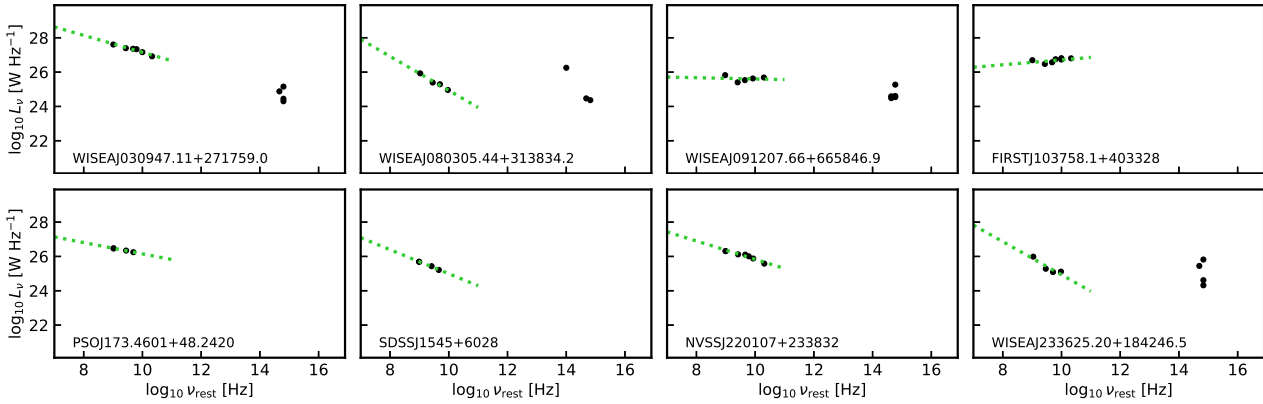


Figure 26. The rest-frame photometry of the remaining Gloude-mans et al. (2023) sample.